Topological nodal surface semimetal states in Sr_5X_3 compounds ($X=$As, Sb, Bi)

Muhammad Rizwan Khan,[1,2] Kun Bu,[1,2] Jian-Tao Wang ●,[1,2,3,*] and Changfeng Chen ●[4]

[1]*Beijing National Laboratory for Condensed Matter Physics, Institute of Physics, Chinese Academy of Sciences, Beijing 100190, China*
[2]*School of Physical Sciences, University of Chinese Academy of Sciences, Beijing 100049, China*
[3]*Songshan Lake Materials Laboratory, Dongguan, Guangdong 523808, China*
[4]*Department of Physics and Astronomy, University of Nevada, Las Vegas, Nevada 89154, USA*

Topological nodal surface semimetals are a class of materials characterized by degenerate conduction and valence bands on closed nodal surfaces in the Brillouin zone that are protected by crystalline symmetries. These materials attract considerable attention for exhibiting intriguing, topologically driven quantum phenomena that are fundamentally interesting and practically useful. Here we identify by systematic *ab initio* calculations and topological quantum chemistry analysis prominent topological nodal surface semimetal states in $Sr_5X_3(X =$ As, Sb, Bi) compounds in hexagonal $P6_3/mcm$ (D_{6h}^3) symmetry. These nodal surface states comprise degenerate the highest occupied band and the lowest unoccupied band that overlap in a single band at the $k_z = \pm\pi$ plane and are protected by time-reversal and nonsymmorphic twofold screw rotation symmetry. Topological quantum chemistry theory analysis reveals a twofold band degeneracy without spin-orbit coupling at the high-symmetry and generic $\boldsymbol{k}$ points located at the $k_z = \pm\pi$ plane, which is formed by the bands of $(A_1 \oplus B_2)@6g$ band representations. Since the compounds studied here have been already experimentally synthesized, the present results have an immediate impact on the experimental detection and characterization of the theoretically predicted topological physics.

I. INTRODUCTION

Searching for new phases of topological materials has been an active area of research in materials physics and related fields, because these materials exhibit interesting fundamental physics phenomena and hold promise for innovative device applications [1–5]. Since the discovery of the topological insulating phase, the concept of nontrivial band topology has been extended to band crossing phases such as topological metals and semimetals [6–10]. After theoretical prediction and experimental realization of Weyl and Dirac semimetals holding nontrivial band crossings in the vicinity of the Fermi level protected by certain symmetries [11–14], topological semimetals have received great attention in materials science and condensed matter physics.

Generally, topological semimetals are classified into different types based on the number of the band degeneracy and the dimensions of the band crossing point in the first Brillouin zone (BZ) [15]. In the former case, the topological semimetals are categorized as Weyl semimetals with isolated Weyl points [11,12], Dirac semimetals with a Dirac node [13,14], and topological nodal line semimetals [16–19] hosting a continuous line of node or ring in the first BZ or higher-order band degeneracy, such as triply degenerate [20] and six- or fourfold band degenerate semimetals [21,22]. In the latter case, these materials can be divided into nodal point semimetals

with zero-dimension band crossing, such as in carbon-based topological semimetals [23–26], nodal line semimetals with one-dimensional band crossing along a certain line [27–31], and nodal surface semimetals with two-dimensional (2D) band crossing in the first BZ [15,32–37].

Based on symmetry protection mechanisms, nodal surface semimetals are further categorized into two types [35]. Type I is protected by inversion, time-reversal, and sublattice symmetry as reported in carbon allotropes [32]. Nodal surface semimetals protected by time-reversal, inversion, and twofold screw symmetry in the absence of spin-orbit coupling (SOC) are termed as type-II nodal surface semimetals [35], which were first proposed to exist in hexagonal BaMX_3 ($M = $ V, Nb, and Ta; $X = $ S or Se) [33] systems, where a single nodal surface is robust without SOC and converted to a so-called Dirac nodal line with SOC. Later on, nodal surface semimetals were reported in K_6YO_4 [35] and a family of $X(MoS)_3(X = $ K, Rb, and Cs) compounds [36], in which a considerable band gap opens with the inclusion of SOC. More recently, spin-polarized type-II nodal loop and nodal surface states have been reported in a $XTiO_2(X = $ Li, Na, K, Rb) family of hexagonal compounds [15]. Meanwhile nodal surface semimetals along with a nodal loop have been investigated in the Ti_3Al family of materials [38] and $Zr_3X(X = $ Al, Ga, In) compounds. These topological semimetal states are expected to hold interesting topological physics and potential device applications. To investigate these features, from the materials point of view, the main conditions are that the band degeneracy should be close to the Fermi level and there should be no

*wjt@aphy.iphy.ac.cn

extra bands nearby. In addition, for experimental realization and practical application, the material should be stable and easy to synthesize. To meet these requirements, there is an urgent need to identify materials suitable for studying nodal surface topological semimetal states.

In this work, we examine binary compounds $Sr_5X_3(X =$ As, Sb, Bi) that have been experimentally synthesized, and their crystal structures are characterized in hexagonal phase with $P6_3/mcm$ (D_{6h}^3) symmetry [39–41]. Based on *ab initio* calculations and topological quantum chemistry (TQC) [42] theory analysis, we identify a topological nodal surface semimetal state in these compounds. The nodal surface state is formed by the crossing of the highest occupied band and the lowest unoccupied bands at the $k_z = \pm\pi$ plane and is protected by time-reversal symmetry and nonsymmorphic twofold screw rotation symmetry without SOC. The TQC theory analysis shows that there is a twofold band degeneracy without SOC at the high-symmetry and generic k points located at the $k_z = \pm\pi$ plane that is formed by the bands of $(A_1 \oplus B_2)@6g$ band representations. With the consideration of SOC, a very small (about ∼2.5 meV) band gap opens in the generic k-point area, but a fourfold band degeneracy remains along the high-symmetry A-H and H-L k paths to form a nodal line structures. These results reveal an excellent nodal surface state (or nodal line state with SOC) in a series of experimentally synthesized materials.

II. COMPUTATIONAL METHODS

Our *ab initio* calculations were performed based on density functional theory (DFT) as implemented in the Vienna *ab initio* simulation package (VASP) [43]. The projector augmented wave (PAW) [44] method was employed with valence electrons of $4s^24p^64d^05s^2$ for Sr, $4s^24p^3$ for As, $5s^25p^3$ for Sb, and $6s^26p^3$ for Bi. The generalized gradient approximation (GGA) developed by Perdew, Burke, and Ernzerhof (PBE) [45] was used as the exchange-correlation functional. A $4 \times 4 \times 5$ Monkhorst-Pack grid of Brillouin zone (BZ) sampling was used, and an energy cutoff of 500 eV was set for the plane-wave basis. The structures were fully relaxed until the total energy difference is less then 10^{-6} eV, and convergence criteria for atomic forces was set to be 10^{-3} eV/Å. The electronic band structures and density of states are calculated by the modified Becke-Johnson (mBJ) [46] functional.

III. RESULTS AND DISCUSSION

Figures 1(a) and 1(b) show the hexagonal crystalline structure of the binary compounds $Sr_5X_3(X =$ As, Sb, Bi) in $P6_3/mcm$ $(D_{6h}^3$, space group No. 193) symmetry. The unit cell contains four Sr_1 atoms occupying the $4d(1/3, 2/3, 1/2)$ Wyckoff positions, six Sr_2 atoms occupying the $6g(x, x, 1/4)$ Wyckoff positions, and six X (As, Sb, Bi) atoms occupying three inequivalent $6g(x, x, 3/4)$ Wyckoff positions. The calculated equilibrium lattice parameters and Wyckoff positions for these compounds are listed in Table I, compared with experimental values [39–41]. It is worth noting that in the crystal structure of Sr_5X_3 compounds, there is a twofold screw rotation symmetry $S_{2z} : (x, y, z) \rightarrow (-x, -y, z + \frac{1}{2})$, which is a nonsymmorphic symmetry involving a twofold rotational
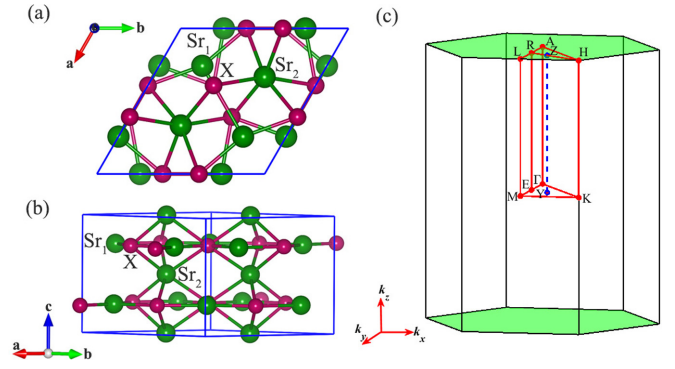
FIG. 1. (a), (b) Top and side views of the unit cell of crystalline structure of hexagonal $Sr_5X_3(X =$ As, Sb, Bi) compounds in $P6_3/mcm$ $(D_{6h}^3$, No. 193) symmetry. The metal atom (Sr) occupies two inequivalent $6g(x, x, 1/4)$ and $4d(1/3, 2/3, 1/2)$ positions, while pnictogen atoms (As, Sb, Bi) occupy the $6g(x, x, 3/4)$ Wyckoff positions. (c) The bulk BZ of the hexagonal Sr_5X_3 compounds with several high-symmetry k points indicated, including Γ (0.0, 0.0, 0.0), M (0.5, 0.0, 0.0), K(1/3, 1/3, 0.0), H (1/3, 1/3, 0.5), A(0.0, 0.0, 0.5), and L (0.5, 0.0, 0.5); R (0.25, 0.0, 0.50) and E (0.25, 0.0, 0.0) are the midpoints along A-L and Γ-M, respectively. Two generic k points Y (0.277, 0.111, 0.0) and Z (0.277, 0.111, 0.5) are at the center of the triangles Γ-M-K and A-H-L, respectively. The red lines highlight the high-symmetry k path. The shaded regions showcase the nodal surface on the $k_z = \pm\pi$ plane.

symmetry (C_2) and a translational symmetry along the [001] direction, and it plays an important role in the nodal surface states protection.

The bulk BZ with high-symmetry k points and k path is given in Fig. 1(c). The electronic band structures and electron density states of these $Sr_5X_3(X =$ As, Sb, Bi) compounds are depicted in Fig. 2. It is seen in Figs. 2(a)–2(c) that the electronic band structures for all three compounds exhibit similar semimetallic features. Near the Fermi level (E_F), the highest valence band (HVB) and the lowest conduction band (LCB) are fully degenerate only along the A-H-L high-symmetry k paths. We have also added two high-symmetry k points R and E at the midpoint of the A–L and Γ-M lines, and a generic

TABLE I. Calculated equilibrium lattice parameters (a, c) and Wyckoff positions for $Sr_5X_3(X =$ As, Sb) compounds, compared to available experimental data [39–41].

Compound	Method	a(Å)	c(Å)	Wyckoff positions	x
Sr_5As_3	PBE	9.05	7.34	$4d(1/3, 2/3, 1/2)$	
				$6g(x, x, 1/4)$	0.745
				$6g(x, x, 3/4)$	0.612
	Exp [39–41]	8.93	7.33		
Sr_5Sb_3	PBE	9.60	7.48	$4d(1/3, 2/3, 1/2)$	
				$6g(x, x, 1/4)$	0.748
				$6g(x, x, 3/4)$	0.609
	Exp [40,41]	9.51	7.43		
Sr_5Bi_3	PBE	9.78	7.59	$4d(1/3, 2/3, 1/2)$	
				$6g(x, x, 1/4)$	0.749
				$6g(x, x, 3/4)$	0.606
	Exp [41]	9.65	7.53		
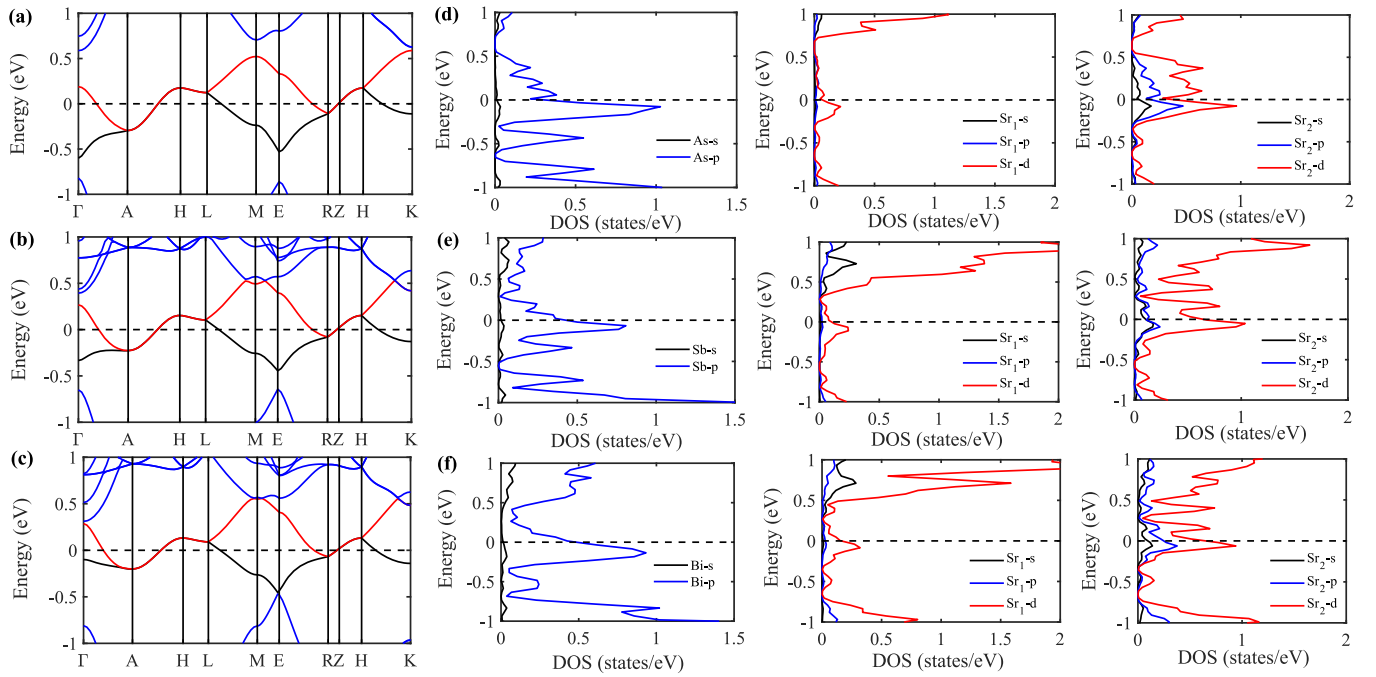
FIG. 2. Calculated electronic band structures without SOC for (a) Sr_5As_3, (b) Sr_5Sb_3, and (c) Sr_5Bi_3 at equilibrium lattice parameters along several high-symmetry directions using the mBJ functional. Calculated partial DOS without SOC for (d) Sr_5As_3, (e) Sr_5Sb_3, and (f) Sr_5Bi_3. The high-symmetry k points are given in Fig. 1(c). The Fermi level is set to zero.

k point Z at the center of the triangle A-H-L. Here, along the R-Z-H k path, a linear band crossing can be clearly observed. This is in agreement with the notion that the antiunitary symmetry ($S_{2z}\mathcal{T}$) guarantees a nodal surface at the $k_z = \pm\pi$ plane [33,35]. It is noted that there is an energy variation in the degenerate band regions along the A-H-L k paths in the ranges of -0.296 eV ~ 0.174 eV for Sr_5As_3, -0.207 eV ~ 0.152 eV for Sr_5Sb_3, and -0.103 eV ~ 0.132 eV for the Sr_5Bi_3 compound. Figures 2(d)–2(f) show the partial density of states (DOS) for Sr_5X_3 compounds. It can be seen that near the Fermi level the electronic behaviors in these compounds are mainly contributed by the p orbitals of X (As, Sb, Bi) atoms and the d orbitals of Sr_2 atoms, with metallic bonds between the Sr_2 and X atoms, such that they show semimetallic properties. The metallic bond grows slightly stronger from As($4p$), Sb($5p$), to Bi($6p$), due to which the flatness of the degenerate bands increases accordingly [see Figs. 2(a)–2(c)]. As a result, in these three compounds, the bands near the Fermi level are mainly contributed by the p orbitals of X (As, Sb, Bi) atoms and the d orbitals of Sr_2 atoms, which are located at $6g(x, x, 1/4)$ and $6g(x, x, 3/4)$ Wyckoff positions, respectively, and this information is important for deducing the elementary band representations (EBRs) of these compounds.

To further check the degeneracy of the LCB and HVB, we plot the three-dimensional (3D) band structures for these compounds. Since the A-H-L k path lies along the $k_z = \pm\pi$ plane, we fix the value of k_z and change the values of k_x and k_y. It is observed that the HVB and LCB are completely overlapping in a single band at the $k_z = \pm\pi$ for the Sr_5As_3 compound, as shown in Fig. 3(a), which corresponds to the nodal surface or, equivalently, to the Dirac nodal points contained in this surface. This band degeneracy is lifted when there is a slight deviation from the $k_z = \pm\pi$ plane; for instance, at

$k_z = \pm0.9\pi$, the conduction and valence bands are separated from each other as depicted in Fig. 3(b). Meanwhile, similar results are obtained for Sr_5Sb_3 and Sr_5Bi_3 (see Fig. S1 in the Supplemental Material [47]).

To better understand the formation mechanism of the nodal surface states in the $k_z = \pm\pi$ plane for Sr_5X_3($X = $ As, Sb, Bi) compounds, we have also calculated the band structures along different high-symmetry k paths perpendicular to the $k_z = \pm\pi$ plane, as shown in Fig. 4. The generic k points Y and Z are at the centers of the triangles Γ-M-K and A-H-L, respectively. Calculated band structures along the different k paths perpendicular to the $k_z = \pm\pi$ plane for Sr_5As_3 [see Figs. 4(a)–4(e)], Sr_5Sb_3 [see Figs. 4(f)–4(j)], and Sr_5Bi_3 [see Figs. 4(k)–4(o)] compounds indicate that there is a linear band crossing between the HVB and LCB bands in all these
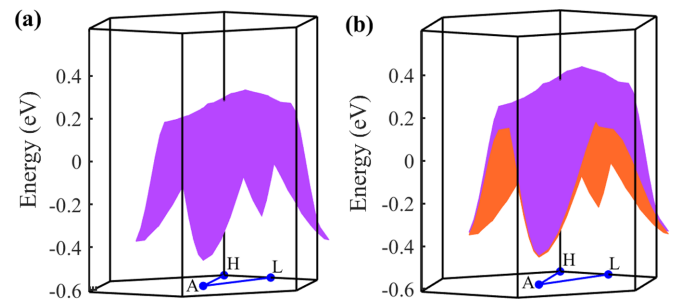
FIG. 3. Calculated three-dimensional band structure along the A-H-L k path in the $k_z = \pm\pi$ (a) and $k_z = \pm0.9\pi$ (b) for Sr_5As_3. Only the valence and conduction bands are shown, and they completely overlap with each other in a single band in the $k_z = \pm\pi$ plane (a), while a gap can be seen between the two bands in $k_z = \pm0.9\pi$ (b).
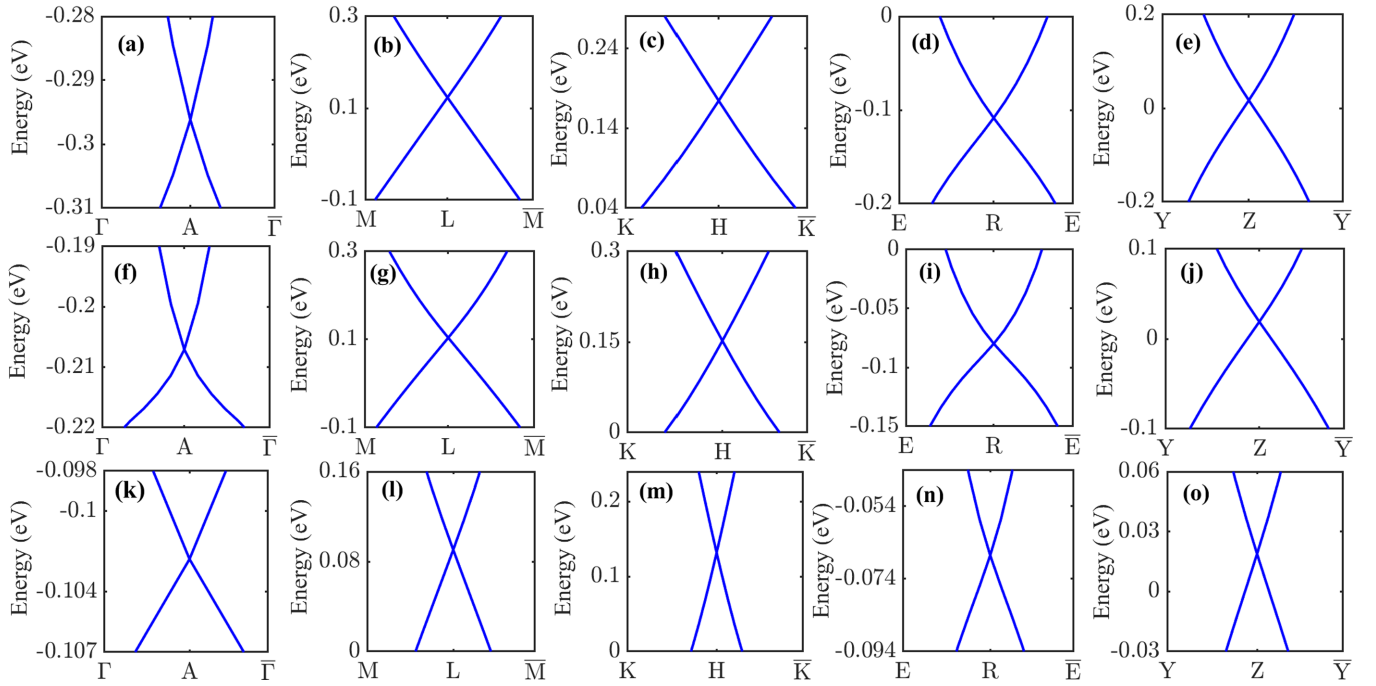
FIG. 4. Electronic band structures near the Fermi level without SOC for Sr_5As_3 (a)–(e), Sr_5Sb_3 (f)–(j), and Sr_5Bi_3 (k)–(o) along the $\boldsymbol{k}$ path perpendicular to the $k_z = \pm\pi$ plane. Here, Z and Y are two generic $\boldsymbol{k}$ paths, which are at the centers of the triangles Γ-M-K and A-H-L, respectively, while high-symmetry points E and R are the midpoints along A-L and Γ-M, respectively.

compounds. It is clearly seen that the band crossing point for every $\boldsymbol{k}$ path is exactly located at the center of the path, which corresponds to a specific nodal point in the $k_z = \pm\pi$ plane. The presence of the linear band crossing along the $\boldsymbol{k}$ paths perpendicular to the $k_z = \pm\pi$ plane confirms the twofold band degeneracy between the valance and conduction bands at the $k_z = \pm\pi$ plane, signifying the nodal surface states in these compounds. Moreover, the existence of nodal surface states in Sr_5X_3 compounds are protected by a combination of the twofold screw rotational (S_{2z}) symmetry and time-reversal symmetry ($\mathcal{T}$), satisfying the relation $(S_{2z}\mathcal{T})^2 = e^{-ik_z}$ without SOC. A more detailed symmetry analysis about the nodal surface states can be found in Refs. [33,35].

TQC theory [42] is a technique for elucidating the properties of topological materials. An electronic band can be characterized by its band representations (BRs). A BR $\rho@q$ is formed by the band of ρ irreducible representation (irrep) centered at the q Wyckoff site. Suppose a set of bands satisfies the "compatibility relations" in group theory but cannot be decomposed into direct sums of the related atomic insulators. Such a scenario indicates the presence of nontrivial topological bands. The existence of nodal surfaces in Sr_5X_3 compounds along the $k_z = \pm\pi$ plane can also be confirmed based on the TQC analysis. The irreps at the Γ, M, K, A, H, L, R, and E high-symmetry points and a generic point Z for highest occupied and lowest unoccupied bands are calculated with the irvsp code [49] and listed in Table II. It is seen that the irrep at A, L, H, and R high-symmetry points are A1(2), L1(2), H1H3(2), and R1(2), respectively, and the result at the Z generic point is Z1Z3(2), which exhibits a 2D representation, thus supporting a twofold band degeneracy. Comparing with the above partial DOS analysis, these two bands should come from the p orbitals of X (As, Sb, Bi) atoms

and the d orbitals of Sr_2 atoms, located at $6g(x, x, 3/4)$ and $6g(x, x, 1/4)$ Wyckoff positions, respectively, and the EBR of these degenerate bands should be $(A_1 \oplus B_2)@6g$. These irreps data clearly show that there is a band degeneracy between the highest occupied and lowest unoccupied bands near E_F at the A, L, H, R, and Z $\boldsymbol{k}$ points located on the $k_z = \pm\pi$ plane. On the other hand, the irreps at Γ, M, K, and E $\boldsymbol{k}$ points are $\Gamma_2^-(1)$ and $\Gamma_4^+(1)$, $M_1^+(1)$ and $M_4^+(1)$, $K_1(1)$ and $K_5(1)$, E3(1) and E4(1), for the HVB and LCB, respectively. The EBR of these two HVB and LCB bands should be $(A_1 \oplus B_2)@6g$ and $A_1@6g$, respectively. These irreps data indicate that there is no band degeneracy between the highest occupied and lowest unoccupied bands near E_F at Γ, M, K, and E $\boldsymbol{k}$ points.

We finally discuss the effect of SOC. The electronic band structures for Sr_5X_3 (As, Sb, Bi) compounds with the consideration of SOC are depicted in Fig. S2 in Supplemental Material [47]. The calculated results indicate that the SOC-induced gaps along the R-Z-H $\boldsymbol{k}$ points are vanishingly small (about $1 \sim 2.5$ meV) in these compounds. Meanwhile, along the high symmetry A-H and H-L $\boldsymbol{k}$ paths, the energy bands remain fourfold degenerate (counting both spin and orbital degrees of freedom), forming a so-called nodal line structure that is protected by the nonsymmorphic twofold screw rotation symmetry with an addition of mirror symmetry [15,33]. In addition, TQC analysis also confirms the fourfold degeneracy along the A-H and H-L $\boldsymbol{k}$ paths with SOC (see Table S1 in Supplemental Material [47]).

Recently, based on the TQC [42] and symmetry-based indicator theories [50–53], several databases [54–56] for 3D nonmagnetic topological materials have been established. In the topological material database [57,58], the Sr_5As_3 family of compounds has been identified as topological semimetals with nodal point type band crossings at the high-symmetry A,

TABLE II. The irreducible representations (irreps) and elementary band representations (EBRs) for the HVB and LCB of Sr_5X_3 compounds around the E_F at Γ, M, K, E, A, L, H, R high-symmetry and Z generic $\boldsymbol{k}$ points without considering SOC (see Fig. 2). Here we use the conventions following those in the Bilbao website [48].

Bands	Γ	M	K	E	A	L	H	R	Z	EBRs
HVB	$\Gamma_2^-(1)$	$M_1^+(1)$	K1(1)	E3(1)	A1(2)	L1(2)	H1H3(2)	R1(2)	Z1Z3(2)	$(A_1 \oplus B_2)@6g$
LCB	$\Gamma_4^+(1)$	$M_4^+(1)$	K5(1)	E4(1)						$A_1@6g$

H, and L $\boldsymbol{k}$ points. However, our present results reveal that Sr_5X_3 compounds are good candidates for observing nodal surface semimetal states, and this is a particularly favorable situation considering that these materials have been experimentally synthesized and high-quality samples have been obtained [39–41]. The predicted nodal surface states are close to the Fermi level and formed by the degenerate LCB and HVB with no extraneous bands nearby. The opening of a negligible band gap with SOC along the R-Z-H $\boldsymbol{k}$-path (or generic points) is smaller than the band gaps in previously reported compounds such as $BaVS_3$ [33], $X(MoS)_3(X = K,$ Rb, and Cs) [36], and $Zr_3X(X = Al, Ga, In)$ [37] nodal surface semimetal. Remarkably, we also find that with the inclusion of the SOC effect the nodal surface state is converted to nodal line along the A-H and H-L high-symmetry $\boldsymbol{k}$ paths (or high symmetric $\boldsymbol{k}$ points) to form a nodal line structure, stemming from the protection of the mirror symmetry. Such nodal line structures are quite rare in realistic materials.

IV. SUMMARY

In summary, we have identified by first-principles calculations a topological nodal surface semimetal state in Sr_5X_3 (X = As, Sb, Bi) compounds, which is formed by the crossing of the highest occupied band and the lowest unoccupied bands at the $k_z = \pm\pi$ plane and is protected by time-reversal symmetry and nonsymmorphic twofold screw rotation symmetry without SOC. Partial density of states and elementary band representation analyses show that the twofold band degeneracy at the high-symmetry and generic points is located at the $k_z = \pm\pi$ plane comprising the bands of $(A_1 \oplus B_2)@6g$ band representations. Meanwhile, with the consideration of the SOC effect there is an opening of a very small (about ~ 2.5 meV) band gap, which has little practical impact on the nature of the identified topological nodal surface semimetal state. Our findings expand and enrich exotic nodal surface states and pave the way for further studies of this prominent family of materials for advancing fundamental understanding and exploring potential applications.

[1] A. A. Burkov, M. D. Hook, and L. Balents, Phys. Rev. B **84**, 235126 (2011).

[2] G. E. Volovik, Lect. Notes Phys. **718**, 31 (2007).

[3] J. T. Wang, H. Weng, and C. F. Chen, Adv. Phys. X **4**, 1625724 (2019).

[4] H. Jin, X. Y. Su, N. Ni, and M. Q. Zhi, Annu. Rev. Mater. Res. **49**, 207 (2019).

[5] G. Heng, V. W. F. Jörn, K. Youngkuk, and R. M. Andrew, Annu. Rev. Mater. Res. **49**, 153 (2019).

[6] C. K. Chiu, J. C. Y. Teo, A. P. Schnyder, and S. Ryu, Rev. Mod. Phys. **88**, 035005 (2016).

[7] N. P. Armitage, E. J. Mele, and A. Vishwanath, Rev. Mod. Phys. **90**, 015001 (2018).

[8] M. Z. Hasan and C. L. Kane, Rev. Mod. Phys. **82**, 3045 (2010).

[9] X. L. Qi and S. C. Zhang, Rev. Mod. Phys. **83**, 1057 (2011).

[10] H. Zhang, C. X. Liu, X. L. Qi, X. Dai, Z. Fang, and S. C. Zhang, Nat. Phys. **5**, 438 (2009).

[11] H. Weng, C. Fang, Z. Fang, B. A. Bernevig, and X. Dai, Phys. Rev. X **5**, 011029 (2015).

[12] X. Wan, A. M. Turner, A. Vishwanath, and S. Y. Savrasov, Phys. Rev. B **83**, 205101 (2011).

[13] Z. Wang, H. Weng, Q. Wu, X. Dai, and Z. Fang, Phys. Rev. B **88**, 125427 (2013).

[14] Z. Wang, Y. Sun, X. Q. Chen, C. Franchini, G. Xu, H. Weng, X. Dai, and Z. Fang, Phys. Rev. B **85**, 195320 (2012).

[15] T. Yang, L. Jin, Y. Liu, X. Zhang, and X. Wang, Phys. Rev. B **103**, 235140 (2021).

[16] H. Huang, J. Liu, D. Vanderbilt, and W. Duan, Phys. Rev. B **93**, 201114(R) (2016).

[17] C. Fang, H. Weng, X. Dai, and Z. Fang, Chin. Phys. B **25**, 117106 (2016).

[18] Y. Kim, B. J. Wieder, C. L. kane, and A. M. Rappe, Phys. Rev. Lett. **115**, 036806 (2015).

[19] T. Hyart, R. Ojajärvi, and T. T. Heikkilä, J. Low. Temp. Phys. **191**, 35 (2018).

[20] B. Bradlyn, J. Cano, Z. Wang, M. G. Vergniory, C. Felser, R. J. Cava, and B. A. Bernevig, Science **353**, 6299 (2016).

[21] S. Nie, B. A. Bernevig, and Z. Wang, Phys. Rev. Res. **3**, L012028 (2021).

[22] M. R. Khan, K. Bu, and J. T. Wang, Phys. Chem. Chem. Phys. **23**, 25944 (2021).

[23] H. Weng, Y. Liang, Q. Xu, R. Yu, Z. Fang, X. Dai, and Y. Kawazoe, Phys. Rev. B **92**, 045108 (2015).

[24] J. T. Wang, H. Weng, S. Nie, Z. Fang, Y. Kawazoe, and C. F. Chen, Phys. Rev. Lett. **116**, 195501 (2016).

[25] Y. Cheng, X. Feng, X. T. Cao, B. Wen, Q. Wang, Y. Kawazoe, and P. Jena, Small **13**, 1602894 (2017).

[26] Z. Zhao, Y. Hang, Z. Zhang, and W. Guo, Phys. Rev. B **100**, 115420 (2019).

[27] Z. Z. Li, J. Chen, S. M. Nie, L. F. Xu, H. Mizuseki, H. Weng, and J. T. Wang, Carbon **133**, 39 (2018).

[28] X. Feng, Q. S. Wu, Y. Cheng, B. Wen, Q. Wang, Y. Kawazoe, and P. Jena, Carbon **127**, 527 (2018).

[29] J. T. Wang, C. F. Chen, and Y. Kawazoe, Phys. Rev. B **97**, 245147 (2018).

[30] J. T. Wang, S. Nie, H. Weng, Y. Kawazoe, and C. F. Chen, Phys. Rev. Lett. **120**, 026402 (2018).

[31] J. T. Wang, Y. Qian, H. Weng, E. G. Wang, and C. F. Chen, J. Phys. Chem. Lett. **10**, 2515 (2019).

[32] C. Zhong, Y. Chen, Y. Xie, S. A. Yang, M. L. Cohen, and S. B. Zhang, Nanoscale **8**, 7232 (2016).

[33] Q. F. Liang, J. Zhou, R. Yu, Z. Wang, and H. Weng, Phys. Rev. B **93**, 085427 (2016).

[34] T. Bzdusek and M. Sigrist, Phys. Rev. B **96**, 155105 (2017).

[35] W. Wu, Y. Liu, S. Li, C. Zhong, Z. M. Yu, X. L. Sheng, Y. X. Zhao, and S. A. Yang, Phys. Rev. B **97**, 115125 (2018).

[36] T. Yang and X. Zhang, J. Mater. Chem. C **8**, 9046 (2020).

[37] H. Xu, H. Xi, and Y. C. Gao, Front. Chem. **8**, 608398 (2020).

[38] X. Zhang, Z. M. Yu, Z. Zhu, W. Wu, S. S. Wang, X. L. Sheng, and S. A. Yang, Phys. Rev. B **97**, 235150 (2018).

[39] B. Better, A. Hütz, and G. Nagorsen, Z. Metallkd. **67**, 118 (1976).

[40] G. Bruzzone, E. Franceschi, and F. J. Merlo, J. Less Common Met. **60**, 59 (1978).

[41] L. Escamilla, E. A. Corbett, and D. John, Chem. Mater. **18**, 4782 (2006).

[42] B. Bradlyn, L. Elcoro, J. Cano, M. Vergniory, Z. Wang, C. Felser, M. Aroyo, and B. A. Bernevig, Nature (London) **547**, 298 (2017).

[43] G. Kresse and J. Furthmüller, Phys. Rev. B **54**, 11169 (1996).

[44] P. E. Blöchl, Phys. Rev. B **50**, 17953 (1994).

[45] J. P. Perdew, K. Burke, and M. Ernzerhof, Phys. Rev. Lett. **77**, 3865 (1996).

[46] A. D. Becke and E. R. Johnson, J. Chem. Phys. **124**, 221101 (2006).

[47] See Supplemental Material at http://link.aps.org/supplemental/10.1103/PhysRevB.105.245152 for the three-dimensional band structures for Sr_5Sb_3 and Sr_5Bi_3 (Fig. S1); the electronic band structures of M_5X_3 compounds with SOC (Fig. S2); and the irreps and EBRs for the degenerate bands of Sr_5X_3 compounds at the high-symmetry A, L, H k points with SOC (Table S1). The Supplemental Material includes Refs. [15,33,48].

[48] L. Elcoro, B. Bradlyn, Z. Wang, M. G. Vergniory, J. Cano, C. Felser, B. A. Bernevig, D. Orobengoa, G. de la Flor, and M. I. Aroyo, J. Appl. Cryst. **50**, 1457 (2017).

[49] J. Gao, Q. Wu, C. Persson, and Z. Wang, Comput. Phys. Commun. **261**, 107760 (2021).

[50] H. C. Po, A. Vishwanath, and H. Watanabe, Nat. Commun. **8**, 50 (2017).

[51] Z. Song, T. Zhang, Z. Fang, and C. Fang, Nat. Commun. **9**, 3530 (2018).

[52] Z. Song, T. Zhang, and C. Fang, Phys. Rev. X **8**, 031069 (2018).

[53] J. Kruthoff, J. de Boer, J. van Wezel, C. L. Kane, and R. J. Slager, Phys. Rev. X **7**, 041069 (2017).

[54] T. Zhang, Y. Jiang, Z. Song, H. Huang, Y. He, Z. Fang, H. Weng, and C. Fang, Nature (London) **566**, 475 (2019).

[55] F. Tang, H. C. Po, A. Vishwanath, and X. Wan, Nature (London) **566**, 486 (2019).

[56] M. G. Vergniory, L. Elcoro, C. Felser, N. Regnault, B. Andrei Bernevig, and Z. Wang, Nature (London) **566**, 480 (2019).

[57] See www.topologicalquantumchemistry.org.

[58] M. G. Vergniory, B. J. Wieder, L. Elcoro, S. S. P. Parkin, C. Felser, B. Andrei Bernevig, and N. Regnault, Science **376**, 6595 (2022).